EXTENDED PDF FORMAT
SPONSORED BY
usb
Products from Affymetrix
www.usbweb.com

Temperature-Induced Hydrophobic-Hydrophilic Transition Observed by Water Adsorption

Hai-Jing Wang, *et al.*

Science **322**, 80 (2008);
DOI: 10.1126/science.1162412

The following resources related to this article are available online at www.sciencemag.org (this information is current as of October 3, 2008):

Updated information and services, including high-resolution figures, can be found in the online version of this article at:
http://www.sciencemag.org/cgi/content/full/322/5898/80

Supporting Online Material can be found at:
http://www.sciencemag.org/cgi/content/full/322/5898/80/DC1

This article **cites 28 articles**, 4 of which can be accessed for free:
http://www.sciencemag.org/cgi/content/full/322/5898/80#otherarticles

This article appears in the following **subject collections**:
Chemistry
http://www.sciencemag.org/cgi/collection/chemistry

Information about obtaining **reprints** of this article or about obtaining **permission to reproduce this article** in whole or in part can be found at:
http://www.sciencemag.org/about/permissions.dtl

Downloaded from www.sciencemag.org on October 3, 2008

Science (print ISSN 0036-8075; online ISSN 1095-9203) is published weekly, except the last week in December, by the American Association for the Advancement of Science, 1200 New York Avenue NW, Washington, DC 20005. Copyright 2008 by the American Association for the Advancement of Science; all rights reserved. The title *Science* is a registered trademark of AAAS.

at half maximum, 500 mW) resulted in a dramatic acceleration in overall rate (90 min) as compared with the use of a typical household 15-W fluorescent bulb (6 hours), which operates with a wide spectral window (~400 to 700 nm). The use of the same 465-nm photon source in the absence of Ru(bpy)$_3^{2+}$ resulted in only trace product formation (<5%) (*28*). These experiments provide strong evidence of the participation of the *Ru(bpy)$_3^{2+}$ (**2**) excited state in the catalytic cycle.

With respect to our luminescence quenching studies, it has long been established that certain electron-deficient C–Br bonds can quench the emission intensity of *Ru(bpy)$_3^{2+}$ by SET (*29*). However, we did not observe a decrease in *Ru(bpy)$_3^{2+}$ luminescence in the presence of α-bromoacetophenone or diethyl bromomalonate, a result that negates the possibility that *Ru(bpy)$_3^{2+}$ (**2**) is participating as a reductant in our tandem catalysis sequence. In contrast, enamine **8** (pregenerated in stoichiometric quantities) does decrease the *Ru(bpy)$_3^{2+}$ emission intensity with a small but significant Stern-Volmer constant of 10 M^{-1} (see fig. S1) (*30*). These observations collectively support our mechanistic proposal that the *Ru(bpy)$_3^{2+}$ (**2**) excited state behaves as an oxidant in our photoredox cycle.

We have also gained circumstantial evidence that enamine **8** is the organocatalytic intermediate that participates in the key bond-forming step. More specifically, exposure of 2-phenylcyclopropyl acetaldehyde to our standard reaction protocol resulted in clean conversion (83% yield) to the corresponding alkylation product (see supporting online material). Failure of this radical clock substrate to undergo cyclopropyl ring opening clearly indicates that a 3π electron SOMO activated intermediate is not operative in the organocatalytic cycle.

References and Notes

1. K. Kalyanasundaram, *Coord. Chem. Rev.* **46**, 159 (1982).
2. A. Juris *et al*., *Coord. Chem. Rev.* **84**, 85 (1988).
3. P. Renaud, M. P. Sibi, Eds., *Radicals in Organic Synthesis* (Wiley-VCH, Weinheim, Germany, 2001).
4. A. Berkessel, H. Gröger, Eds., *Asymmetric Organocatalysis: From Biomimetic Concepts to Applications in Asymmetric Synthesis* (Wiley-VCH, Weinheim, Germany, 2005).
5. P. I. Dalko, Ed., *Enantioselective Organocatalysis: Reactions and Experimental Procedures* (Wiley-VCH, Weinheim, Germany, 2007).
6. T. D. Beeson, A. Mastracchio, J. B. Hong, K. Ashton, D. W. C. MacMillan, *Science* **316**, 582 (2007); published online 28 March 2007 (10.1126/science. 1142696).
7. H. Jang, J. B. Hong, D. W. C. MacMillan, *J. Am. Chem. Soc.* **129**, 7004 (2007).
8. H. Kim, D. W. C. MacMillan, *J. Am. Chem. Soc.* **130**, 398 (2008).
9. A SOMO activation mechanism has also been reported for the α-oxidation of aldehydes (*10*).
10. M. Sibi, M. Hasegawa, *J. Am. Chem. Soc.* **129**, 4124 (2007).
11. H. B. Gray, J. R. Winkler, *Annu. Rev. Biochem.* **65**, 537 (1996).
12. An intramolecular α-formyl alkylation has been reported (*13*).
13. N. Vignola, B. List, *J. Am. Chem. Soc.* **126**, 450 (2004).
14. For a catalytic enantioselective alkylation of racemic α-bromoesters, see (*15*).
15. X. Dai, N. A. Strotman, G. C. Fu, *J. Am. Chem. Soc.* **130**, 3302 (2008).
16. P. Renaud, S. Schubert, **1990**, *Synlett* 624 (1990).
17. G. A. Russell, K. Wang, *J. Org. Chem.* **56**, 3475 (1991).
18. C. R. Bock *et al*., *J. Am. Chem. Soc.* **101**, 4815 (1979).
19. Value was corrected from the Ag/Ag$^+$ClO$_4^-$ electrode (*20*).
20. D. D. Tanner, H. K. Singh, *J. Org. Chem.* **51**, 5182 (1986).
21. Ru(bpy)$_3^+$ has previously been shown to reduce phenacyl bromide (*22*).
22. S. Fukuzumi, S. Mochizuki, T. Tanaka, *J. Phys. Chem.* **94**, 722 (1990).
23. D. D. M. Wayner, J. J. Dannenberg, D. Griller, *Chem. Phys. Lett.* **131**, 189 (1986).
24. The possibility of direct one-electron reduction of the α-bromocarbonyl by the α-amino radical as a propagation step cannot be excluded.
25. DFT calculations were performed with the use of B3LYP/6-311+G(2d,2p)//B3LYP/6-31G(d).
26. A conformer that positions the enamine olefin toward the *tert*-butyl group was also found to be energetically relevant in these calculations. Because of the pseudo C_2-symmetric nature of catalyst **6**, this enamine conformer also exists with the *Si* face open and the *Re* face blocked in a manner similar to DFT–**8**.
27. Materials and methods are available as supporting material on *Science* Online.
28. No rate enhancement was observed in the absence of Ru(bpy)$_3^{2+}$ with additive bpy or Bu$_4$NCl.
29. S. Oishi, N. Furuta, *Chem. Lett.* **7**, 45 (1978).
30. None of the remaining reaction components (aldehyde, amine catalyst, 2,6-lutidine, or 2,6-lutidinium bromide) quenched *Ru(bpy)$_3^{2+}$.
31. We thank S. Bernhard for his assistance in performing quenching experiments, as well as many insightful discussions. Additionally, we thank T. J. Rainey for performing DFT calculations. Financial support was provided by the NIH General Medical Sciences (grant R01 GM078201-01-01) and gifts from Merck, Amgen, and Bristol-Myers Squibb. D.A.N. is grateful for a NIH National Service Research Award fellowship (F32GM076816).

Supporting Online Material

www.sciencemag.org/cgi/content/full/1161976/DC1
Materials and Methods
Figs. S1 to S3
References

18 June 2008; accepted 8 August 2008
Published online 4 September 2008;
10.1126/science.1161976
Include this information when citing this paper.

Temperature-Induced Hydrophobic-Hydrophilic Transition Observed by Water Adsorption

Hai-Jing Wang, Xue-Kui Xi, Alfred Kleinhammes, Yue Wu*

The properties of nanoconfined and interfacial water in the proximity of hydrophobic surfaces play a pivotal role in a variety of important phenomena such as protein folding. Water inside single-walled carbon nanotubes (SWNTs) can provide an ideal system for investigating such nanoconfined interfacial water on hydrophobic surfaces, provided that the nanotubes can be opened without introducing excess defects. Here, we report a hydrophobic-hydrophilic transition upon cooling from 22°C to 8°C via the observation of water adsorption isotherms in SWNTs measured by nuclear magnetic resonance. A considerable slowdown in molecular reorientation of such adsorbed water was also detected. The observed transition demonstrates that the structure of interfacial water could depend sensitively on temperature, which could lead to intriguing temperature dependences involving interfacial water on hydrophobic surfaces.

Water in the immediate vicinity of hydrophobic surfaces plays a crucial role in various important phenomena such as the folding and activity of proteins (*1*, *2*), but experimental signatures of these water layers have proven difficult to obtain. One possibility is that the structures and dynamics of nanoconfined interfacial water could possess distinctive temperature dependences (analogous perhaps to the anomalous density maximum manifested by bulk water at 4°C). A temperature dependence in the properties of interfacial water could be important for various processes, such as the cold denaturation of proteins (*2*).

Single-walled carbon nanotubes (SWNTs) provide a model system for investigating the properties of nanoconfined interfacial water (*3*–*9*). Because each nanotube with diameter of 1.4 nm can only accommodate one layer of water molecules on their inside surface (*5*), the behavior of adsorbed water inside such SWNTs could provide important insight into the properties of nanoconfined interfacial water. A previous theoretical study showed that water could fill the interior of carbon nanotubes through favorable structural effects on the local excess chemical potential (*3*). This result implies that water could be adsorbed inside SWNTs below saturated vapor pressure, as demonstrated by previous studies (*10*, *11*). However, in those studies, the defect density and principal adsorption sites (PAS), known to alter water adsorption isotherms in activated carbon (*12*), were likely too high to reveal the intrinsic adsorption properties of SWNTs. Water

---

Department of Physics and Astronomy, University of North Carolina, Chapel Hill, NC 27599–3255, USA.

*To whom correspondence should be addressed. E-mail: yuewu@physics.unc.edu

adsorption isotherms in SWNTs depend on both the interaction with the surface and the structure of adsorbed water, which could depend on temperature. Here, we report a hydrophobic-hydrophilic transition upon cooling from 22.1°C to 8.0°C, revealed by water adsorption isotherms on the inside surface of low-defect SWNTs. Strong evidence is provided for the formation of monolayer water inside SWNTs at 8.0°C. Nuclear magnetic resonance (NMR) studies of the dynamics of reorientation of nanoconfined water molecules are shown to be much slower than in bulk water. In addition to various important biological processes, this new phenomenon could also shed light on the intrinsic adsorption mechanism of water in nanoporous carbon (*12*, *13*).

We synthesized SWNTs by laser ablation using 0.6 weight percent (each) Ni/Co as catalysts. The raw material was purified by refluxing in 20% H_2O_2 solution at 100°C for 12 hours and rinsing in CS_2 and then in methanol. The purified SWNTs were then annealed at 800°C. The tube diameter of 1.4 nm was determined from the Raman spectrum. Details of the sample preparation were described previously (*14*). The transmission electron microscope (TEM) image of the SWNTs is shown in fig. S1 (*15*). SWNTs after annealing usually have end caps that prevent the guest molecules from being adsorbed inside. Several techniques can be used to open the ends of SWNTs. In our previous study, etching by strong acids was used to cut tubes into short segments (*10*, *16*, *17*). Although this method is effective for opening tubes, it introduces a considerable amount of defect sites and functional groups acting as PAS that could have a strong influence on the water adsorption behavior. The high defect density in cut SWNTs could obscure the intrinsic adsorption behavior of SWNTs (*10*).

To reduce the influence of PAS and to reveal the intrinsic adsorption behavior, a much gentler method was adopted here to remove end caps (*18*). The SWNTs were heated at around 350°C in a thermogravimetric analyzer under air flow for more than 20 min until a weight loss of about 3% was reached. The ^{1}H NMR spectrum of ethane (fig. S2) (*15*) adsorbed in such treated SWNTs shows clear signatures of opened SWNTs (*16*, *17*). Water adsorption isotherms were measured by ^{1}H NMR at 0.8 T (34 MHz ^{1}H NMR frequency) equipped with an in situ water loading system with controlled vapor pressure and temperature. The ^{1}H NMR signal of vapor is negligible because of its low pressure (~2 kPa); no bulk water is condensed outside SWNTs below the saturated vapor pressure (P_0). Furthermore, water molecules are too large to access the interstitial sites of 1.4-nm diameter SWNTs bundles (*16*). Thus, the ^{1}H NMR signal is associated predominantly with the water adsorbed inside the SWNTs (*11*). The water content is calibrated by ethane ^{1}H NMR spectra as described in details elsewhere (*10*, *16*).

The amount of adsorbed water measured by ^{1}H NMR versus the relative pressure P/P_0 at 8.0°C, 18.4°C, and 22.1°C is shown in Fig. 1A. All three isotherms differ substantially from the S-shaped type V isotherm as observed in activated carbon and defective cut SWNTs, where adsorption increases slowly at low relative pressure but increases sharply above P/P_0 = 0.5, quickly reaching the level of saturation (*10*). Such an S-shaped adsorption isotherm in activated carbon is often attributed to PAS (*12*). Figure 1A shows that this ubiquitous sharp increase in the isotherms of activated carbon near P/P_0 = 0.5 is absent in low-defect SWNTs. The isotherm at 22.1°C exhibits a concave pattern as a type III isotherm, typical for clean hydrophobic surfaces with surface-water interactions weaker than water-water interactions (*19*). Interestingly, the isotherm at 8.0°C exhibits a convex pattern, a type II isotherm observed on hydrophilic surfaces (*20*). The isotherm at 18.4°C shows a linear pattern, which is a transitional pattern between the hydrophilic isotherm at 8.0°C and the hydrophobic isotherm at 22.1°C.

The water content was about 15 mmol/g when the relative pressure first reached the saturated pressure of $P/P_0 = 1$. This value is in good agreement with the calculated adsorption capacity of 13 mmol/g when SWNTs are supposed to be completely filled with water. This estimate is made by assuming that the van der Waals diameter of (10, 10) SWNTs is 0.99 nm (*5*) and the density of water is comparable to those at the hydrophobic interface, about 0.9 g/cm^3 (*21*). Further exposure at P/P_0 = 1 will lead to further increase of adsorption caused by condensation outside SWNTs.

More insight can be gained by analyzing the isotherm at 8.0°C with the Dubinin-Radushkevitch-Kaganer equation (*19*). It describes monolayer adsorption, given by

$$\log_{10} x = \log_{10} x_m - D[\log_{10} P_0/P)]^2 \qquad (1)$$

where x is the adsorbed water content, x_m is the monolayer capacity, and D is a constant related to the temperature. A logarithmic plot of the adsorbed water versus $[\log_{10}(P_0/P)]^2$ is shown in Fig. 1C. Using the linear fit of data below the pressure of condensation and extrapolating to $[\log_{10}(P_0/P)]^2 = 0$, the monolayer capacity x_m is evaluated to be 8.7 ± 0.4 mmol/g. This value agrees well with the calculated value of 9.5 mmol/g for monolayer coverage of the inner surface of SWNTs. The monolayer water forms a tubular structure under the confinement of nanotubes, as illustrated in Fig. 1B (*22*). The convex shape of the water adsorption isotherm at 8.0°C and its upward turn at $P/P_0 \approx 0.8$ are also evidences of molecular layering on the adsorbed surface (*23*). This layering effect is commonly seen in liquid films (above the triple point temperature of the bulk liquid) of simple hydrocarbons and inert gases on graphite.

Water adsorption is a process of balancing the chemical potential of the confined water and the vapor. When water is confined in SWNTs, the energy loss from the breaking of hydrogen bonding (~20 kJ/mol) will not be completely compensated by the van der Waals interaction (<15 kJ/mol) (*24*). However, the local excess chemical potential is dominated not by the aver-

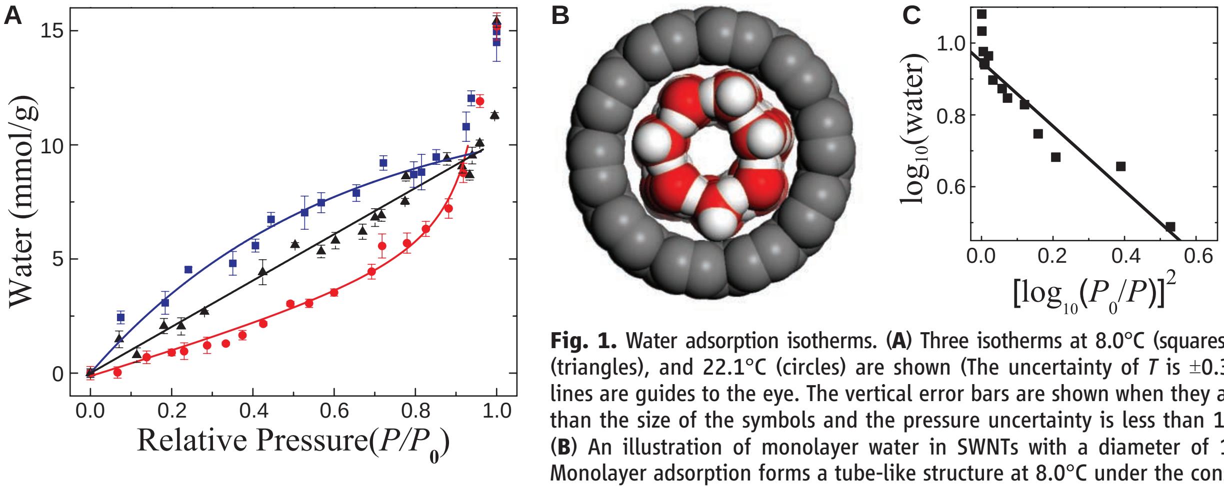

Fig. 1. Water adsorption isotherms. (**A**) Three isotherms at 8.0°C (squares), 18.4°C (triangles), and 22.1°C (circles) are shown (The uncertainty of *T* is ±0.3°C). The lines are guides to the eye. The vertical error bars are shown when they are larger than the size of the symbols and the pressure uncertainty is less than 1% of P_0. (**B**) An illustration of monolayer water in SWNTs with a diameter of 1.36 nm. Monolayer adsorption forms a tube-like structure at 8.0°C under the constraint of SWNTs. (**C**) A logarithmic plot of water content versus $[\log_{10}(P_0/P)]^2$ for the isotherm at 8.0°C, following the Dubbin-Radushkevitch-Kaganer equation.

age binding energy but by the low binding energy part, as determined by

$$\exp(\beta\mu^{ex}) = \langle\exp(\beta u)\rangle = \int p_{bind}(u)\exp(\beta u)du \qquad (2)$$

where $\beta = 1/k_BT$, $p_{\mathrm{bind}}(u)$ is the probability distribution of binding energy u (u <0), and μ^{ex} is the local excess chemical potential defined as the difference between the chemical potential of water and that of an ideal gas under the same condition (*3*).

At 8.0°C, water adsorption proceeds so as to form a monolayer. The binding energy for adsorbed water with an ordered water nanotube structure, as predicted theoretically (*25*, *26*), is expected to be distributed more sharply than in bulk water. States of low binding energy are less frequently occupied. The chemical potential could be lower than that of saturated vapor. Thus, substantial adsorption could happen even at low relative pressure at 8.0°C, as shown in Fig. 1A. At 22.1°C, the adsorbed water in SWNTs could possess a variety of local structures and a broader distribution in binding energy. More states could be located in the low binding energy region, leading to higher chemical potential and an unfavorable condition for adsorption. Thus, much less water was adsorbed in SWNTs at 22.1°C than at 8.0°C.

To investigate the dynamics of adsorbed water molecules, the correlation time of molecular motion was estimated with ^{1}H spin-lattice relaxation time (T_1) and transverse relaxation time (T_2). The ^{1}H T_1 in water is determined by interaction fluctuations induced by molecular motions characterized by a correlation time τ. Assuming that the intramolecular proton-proton dipolar interaction of water molecules dominates the relaxation process, T_1 is given by (*27*)

$$\left(\frac{1}{T_1}\right) = \frac{3\gamma^4\hbar^2}{10r^6}\left(\frac{\tau}{1+\omega_0^2\tau^2} + \frac{4\tau}{1+4\omega_0^2\tau^2}\right) \qquad (3)$$

where γ is the gyromagnetic ratio of proton, $2\pi\hbar$ is the Planck constant, r is the distance between the two hydrogen atoms in a water molecule, and $\omega_0/2\pi$ is the Larmor frequency (34 MHz at 0.8 T). A quantitative relation between T_2 and τ can also be established (*28*).

$$\left(\frac{1}{T_2}\right) = \frac{3\gamma^4\hbar^2}{20r^6} \times \left(3\tau + \frac{5\tau}{1+\omega_0^2\tau^2} + \frac{2\tau}{1+4\omega_0^2\tau^2}\right) \qquad (4)$$

Figure 2C plots the theoretical values of T_1 and T_2 versus τ. The measured T_1 values versus pressure at 8.0°C and 18.4°C are shown in Fig. 2A. The T_1 at 8.0°C is shorter than that of 18.4°C at the same relative pressure until the saturated pressure is reached, where T_1 values at both temperatures converge to the same value. At 8.0°C, T_1 decreases slowly with increasing pressure up to P/P_0 = 1.0. At 18.4°C, however, T_1 decreases slowly with increasing pressure below P/P_0 = 0.8 but decreases rapidly with pressure above P/P_0 = 0.8.

Similarly, at 8.0°C, T_2 (Fig. 2B) increases slowly with pressure up to P/P_0 = 1.0, whereas at 18.4°C, T_2 increases very slowly below P/P_0 = 0.8 but increases sharply above P/P_0 = 0.8. T_2 is longer at 8.0°C than at 18.4°C at low relative pressure and becomes comparable at saturated pressure. This measurement reveals that T_2 is much shorter than T_1. Also, T_2 increases while T_1 decreases with either increasing relative pressure or decreasing temperature. Thus, the measured T_1 values are situated to the right of the T_1 minimum (slow-motion limit), as illustrated in Fig. 2C by the data at P/P_0 = 0.75. The measured T_2 values at P/P_0 = 0.75 are shorter than theoretical predictions, as plotted in Fig. 2C. The theoretical prediction of T_2 considers only intramolecular dipolar interaction and underestimates the relaxation rate $1/T_2$, which also depends on the intermolecular dipolar interactions. The molecular motions under confinement are anisotropic, and the intermolecular dipolar interaction cannot be easily averaged to zero (*29*, *30*).

The correlation time changes from 132 ns when T_1 is 7 ms (18.4°C, P/P_0 = 0.75) to 46 ns when T_1 is 3 ms (8.0°C, P/P_0 = 0.75). They are several orders of magnitude longer than 3.5 ps of bulk water at 20°C (on the left edge of Fig. 2C). The correlation time at 8.0°C is shorter than that at 18.4°C at low relative pressure, and the amount of adsorbed water at a given relative pressure below P/P_0 = 0.9 is different at these two temperatures. The structure and density of adsorbed water are also expected to be different and could lead to the observed difference in the correlation time. The correlation time at these two temperatures did become the same at P/P_0 = 1.0 (26 ns), where the amount of water became comparable. This suggests that the structure is similar at these two temperatures when the SWNTs are filled with water.

Because the intramolecular dipolar interaction dominates the spin-lattice relaxation, the long correlation time τ suggests that there is a substantial slowdown in molecular reorientation. The slowdown of certain dynamics of water in proximity to small hydrophobic groups has been shown previously (*31*). Here, we show a similar slowdown of water reorientation in proximity to an extended nonpolar surface.

Although the hydrophobic effect is widely known to be temperature dependent, our observation demonstrates that such temperature dependence could cause a qualitative change, as manifested by the hydrophobic-hydrophilic transition. At lower temperatures, well-defined layered structures of nanoconfined water on hydrophobic surfaces lead to a narrower probability distribution of the binding energy, making adsorption favorable in terms of the free energy. When such ordered structure is weakened at higher temperature, the distribution of the binding energy broadens, making adsorption unfavorable.

The hydrophobicity should not be considered as an absolute property of a surface under nanoconfinement without considering the structure of interfacial water. The correlation time of water reorientation in SWNTs is determined to be on the order of 10 to 100 ns. This result shows that the dynamics of water reorientation is hin-

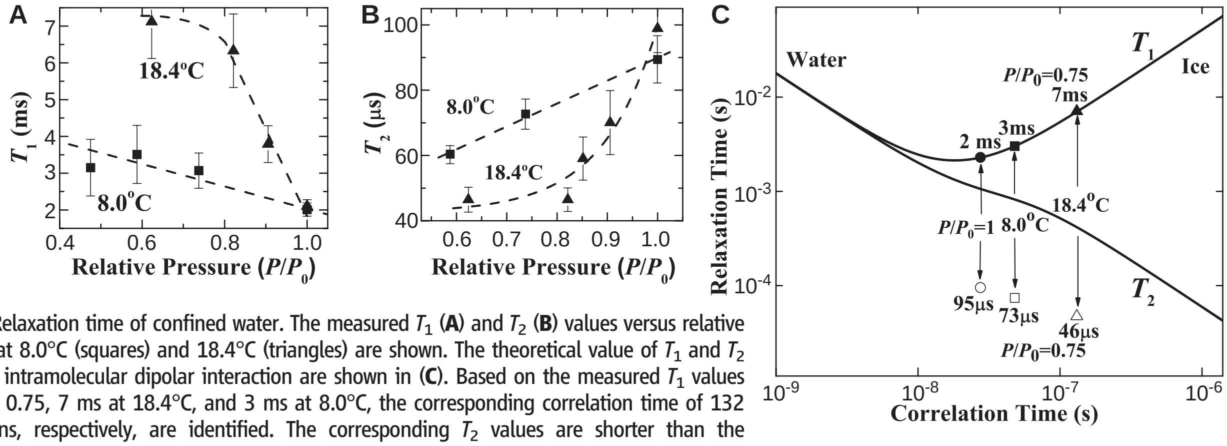

Fig. 2. Relaxation time of confined water. The measured T_1 (**A**) and T_2 (**B**) values versus relative pressure at 8.0°C (squares) and 18.4°C (triangles) are shown. The theoretical value of T_1 and T_2 based on intramolecular dipolar interaction are shown in (**C**). Based on the measured T_1 values at P/P_0 = 0.75, 7 ms at 18.4°C, and 3 ms at 8.0°C, the corresponding correlation time of 132 and 46 ns, respectively, are identified. The corresponding T_2 values are shorter than the theoretically expected values. The correlation time at these two temperatures becomes the same at P/P_0 = 1 (26 ns).

dered compared with bulk water, consistent with the dynamics of water molecules in proximity to small hydrophobic groups (*31*). The confined and interfacial water are prevalent in biological systems, such as the water in ion channels and in proximity to proteins. The affinity change due to temperature-induced structural change of water could be relevant to various phenomena, including in biological systems, such as the cold denaturation of proteins (*2*).

References and Notes

1. D. Chandler, *Nature* **437**, 640 (2005).
2. C. J. Tsai, J. V. Maizel, R. Nussinov, *Crit. Rev. Biochem. Mol. Biol.* **37**, 55 (2002).
3. G. Hummer, J. C. Rasaiah, J. P. Noworyta, *Nature* **414**, 188 (2001).
4. K. Koga, G. T. Gao, H. Tanaka, X. C. Zeng, *Physica A* **314**, 462 (2002).
5. R. J. Mashl, S. Joseph, N. R. Aluru, E. Jakobsson, *Nano Lett.* **3**, 589 (2003).
6. A. I. Kolesnikov *et al.*, *Phys. Rev. Lett.* **93**, 035503 (2004).
7. Y. Maniwa *et al.*, *Chem. Phys. Lett.* **401**, 534 (2005).
8. A. Striolo *et al.*, *Adsorption* **11**, 397 (2005).
9. J. K. Holt *et al.*, *Science* **312**, 1034 (2006).
10. S. H. Mao, A. Kleinhammes, Y. Wu, *Chem. Phys. Lett.* **421**, 513 (2006).
11. Q. Chen *et al.*, *Nano Lett.* **8**, 1902 (2008).
12. R. S. Vartapetyan, A. M. Voloshchuk, *Usp. Khim.* **64**, 1055 (1995).
13. T. Ohba, H. Kanoh, K. Kaneko, *J. Am. Chem. Soc.* **126**, 1560 (2004).
14. X. P. Tang *et al.*, *Science* **288**, 492 (2000).
15. Materials and methods are available as supporting material on *Science* Online.
16. A. Kleinhammes *et al.*, *Phys. Rev. B* **68**, 075418 (2003).
17. H. Z. Geng *et al.*, *Chem. Phys. Lett.* **399**, 109 (2004).
18. Y. Maniwa *et al.*, *Nat. Mater.* **6**, 135 (2007).
19. S. J. Gregg, K. S. W. Sing, *Adsorption, Surface Area, and Porosity* (Academic Press, London, New York, ed. 2, 1982).
20. J. Pires, M. L. Pinto, A. Carvalho, M. B. de Carvalho, *Adsorption* **9**, 303 (2003).
21. T. R. Jensen *et al.*, *Phys. Rev. Lett.* **90**, 086101 (2003).
22. O. Byl *et al.*, *J. Am. Chem. Soc.* **128**, 12090 (2006).
23. D. Beaglehole, H. K. Christenson, *J. Phys. Chem.* **96**, 3395 (1992).
24. G. R. Birkett, D. D. Do, *J. Phys. Chem. C* **111**, 5735 (2007).
25. T. Kurita, S. Okada, A. Oshiyama, *Phys. Rev. B* **75**, 205424 (2007).
26. D. Takaiwa, I. Hatano, K. Koga, H. Tanaka, *Proc. Natl. Acad. Sci. U.S.A.* **105**, 39 (2008).
27. A. Abragam, *The Principles of Nuclear Magnetism* (Clarendon Press, Oxford, 1961).
28. R. Kubo, K. Tomita, *J. Phys. Soc. Jpn.* **9**, 888 (1954).
29. J. P. Korb, S. Xu, J. Jonas, *J. Chem. Phys.* **98**, 2411 (1993).
30. J. Baugh *et al.*, *Science* **294**, 1505 (2001).
31. Y. L. A. Rezus, H. J. Bakker, *Phys. Rev. Lett.* **99**, 148301 (2007).

32. This work was supported by NSF under contract DMR 0513915. We thank O. Zhou for help in SWNTs synthesis.

Supporting Online Material

www.sciencemag.org/cgi/content/full/322/5898/80/DC1
Figs. S1 and S2

26 June 2008; accepted 19 August 2008
10.1126/science.1162412

Atmospheric CO_2 and Climate on Millennial Time Scales During the Last Glacial Period

Jinho Ahn* and Edward J. Brook

Reconstructions of ancient atmospheric carbon dioxide (CO_2) variations help us better understand how the global carbon cycle and climate are linked. We compared CO_2 variations on millennial time scales between 20,000 and 90,000 years ago with an Antarctic temperature proxy and records of abrupt climate change in the Northern Hemisphere. CO_2 concentration and Antarctic temperature were positively correlated over millennial-scale climate cycles, implying a strong connection to Southern Ocean processes. Evidence from marine sediment proxies indicates that CO_2 concentration rose most rapidly when North Atlantic Deep Water shoaled and stratification in the Southern Ocean was reduced. These increases in CO_2 concentration occurred during stadial (cold) periods in the Northern Hemisphere, several thousand years before abrupt warming events in Greenland.

The last glacial period was characterized by abrupt climate and environmental changes on millennial time scales. Prominent examples include abrupt warming and cooling in Greenland ice core records (Dansgaard-Oeschger, or DO, events) (*1*, *2*) and abrupt iceberg discharges in the North Atlantic (Heinrich, or H, events) (*3*), the latter appearing to predate the longest and largest DO events (Fig. 1A). Age synchronization between Greenland and Antarctic ice cores through atmospheric CH_4 variations reveals that Antarctic and Greenlandic temperature are linked, but not in phase (*4*, *5*) (Fig. 1, A, B, and D). Antarctic warming started before warming in Greenland for most of the large millennial events in the records, and Antarctic temperatures began to decline when Greenland rapidly warmed. Model and ice core studies suggest that this link is maintained by changes in meridional overturning circulation (*6*, *7*).

In contrast to the interhemispheric climate link, the relation between atmospheric CO_2 and climate, in the glacial period [~20 to 120 thousand years ago (ka)], has not been as well documented because of scatter in data sets (*8*) and/or chronological uncertainties (*9*). Understanding CO_2 variability is important, however, because of the direct role of CO_2 as a greenhouse gas and the probable influence of changes in ocean circulation on past atmospheric CO_2 concentrations. Here, we provide high-resolution atmospheric CO_2 data from the Byrd ice core (*10*), with a chronology well synchronized with the Greenland ice cores via CH_4 correlation (*4*). The data cover the period of 20 to 90 ka (Fig. 1C), including previously published results for 47 to 65 ka (*11*). We also measured CH_4 in 36 samples from Byrd to better constrain the chronology of the 67- to 87-ka time period [the time of DO-19, 20, and 21 and Antarctic events A5 to A7 (*4*)] (Fig. 1D). Rapid increases in CH_4 concentration are essentially synchronous with abrupt warming in Greenland within decades (*12*–*14*). With CH_4 and CO_2 data from the same core, and in many cases from the same samples, we could directly study the phasing between CO_2 and Greenland temperature variations, circumventing uncertainties due to age differences between ice and gas in ice core records (*12*–*14*).

We call attention to two distinct features of atmospheric CO_2 variations associated with climate changes in the Northern and Southern Hemispheres. First, CO_2 variation is strongly correlated with $\delta^{18}O_{ice}$ in the Byrd core, a proxy for site temperature, but whereas CO_2 remained relatively stable for about 1 to 2 ka after reaching maximum levels associated with peaks in Antarctic warming, Antarctic temperature dropped rapidly (Fig. 1, B and C, and fig. S1). In contrast to the slow decline of CO_2 relative to Antarctic cooling, the onsets of CO_2 increases are generally synchronous with Antarctic warming within data and age uncertainties (fig. S1).

Second, an increase in CO_2 predates, by 2 to 5 ka, the abrupt warming in Greenland associated with DO events, 8, 12, 14, 17, 20 and 21, the largest and longest abrupt events in the Greenland record over this time period (Figs. 1, A and C, and 2) (DO-19 may be an exception, but the timing of the onset of CO_2 rise is difficult to determine). The CO_2 increase slowed just after the abrupt warming of those events. We do not resolve any similar CO_2 variability associated with the shorter DO climate oscillations in the 37- to 65-ka period (DO-9, 11, 13, 15) with the current data set, but small variations associated with the shorter DO cycles cannot be excluded. Between 19 and 37 ka, there are some variations that may be associated with DO events 2 to 7, particularly a CO_2 peak at ~ 28 ka, which may be related to DO-4 and the stadial period preceding it. Higher-resolution data will be needed to further understand this variability.

Models of millennial-scale CO_2 variations suggest that changes in North Atlantic Deep

---

Department of Geosciences, Oregon State University, Corvallis, OR 97331–5506, USA.

*To whom correspondence should be addressed. E-mail: jinhoahn@gmail.com